

PAPER

## Ultra-subwavelength focusing and giant magnetic-field enhancement in a low-loss one-way waveguide based on remanence

To cite this article: Jie Xu *et al* 2020 *J. Opt.* **22** 025003

View the [article online](#) for updates and enhancements.



**IOP | ebooks™**

Bringing you innovative digital publishing with leading voices to create your essential collection of books in STEM research.

Start exploring the collection - download the first chapter of every title for free.

# Ultra-subwavelength focusing and giant magnetic-field enhancement in a low-loss one-way waveguide based on remanence

Jie Xu<sup>1,2,3</sup>, Xiaohua Deng<sup>2</sup>, Hang Zhang<sup>4</sup>, Chiaho Wu<sup>4</sup>, Martijn Wubs<sup>3,5</sup> , Sanshui Xiao<sup>3,5</sup>  and Linfang Shen<sup>2,4</sup> 

<sup>1</sup> College of Material Science and Engineering, Nanchang University, Nanchang 330031, People's Republic of China

<sup>2</sup> Institute of Space Science and Technology, Nanchang University, Nanchang 330031, People's Republic of China

<sup>3</sup> Department of Photonics Engineering, Technical University of Denmark, DK-2800 Kgs. Lyngby, Denmark

<sup>4</sup> Department of Applied Physics, Zhejiang University of Technology, Hangzhou 310023, People's Republic of China

<sup>5</sup> Center for Nanostructured Graphene, Technical University of Denmark, DK-2800 Kgs. Lyngby, Denmark

E-mail: [physzhang@zjut.edu.cn](mailto:physzhang@zjut.edu.cn) and [lfshen@zjut.edu.cn](mailto:lfshen@zjut.edu.cn)

Received 19 September 2019, revised 6 December 2019

Accepted for publication 8 January 2020

Published 22 January 2020



CrossMark

## Abstract

The subwavelength focusing based on surface plasmon polaritons has been widely explored in tapered metallic structures. However, the efficiency of energy localization is relatively weak, largely due to high propagation loss and strong back reflection. Here, we propose a three-dimensional (3D) straight-tapered one-way surface magnetoplasmon (SMP) waveguide with the end surface of  $\sim 10^{-4}\lambda_0 \times 10^{-4}\lambda_0$  to achieve energy focusing in the microwave regime. Due to low propagation loss of SMP, we achieve huge magnetic field enhancement in such an ultra-subwavelength area, by five orders of magnitude. Instead of using an external static magnetic field, our proposed SMP waveguide relies on remanence, which is very convenient for operating practical 3D applications. These results show promising applications in magnetic-field enhancing or quenching fluorescence, luminescence or nonlinearity of two-dimensional materials, novel scanning near-field microwave microscopy and energy storage.

Keywords: one-way waveguide, remanence, magnetic field enhancement, subwavelength focusing

(Some figures may appear in colour only in the online journal)

## 1. Introduction

Similar to the chiral edge states founded in the quantum-Hall effect [1], one-way propagation of electromagnetic (EM) modes have increasingly attracted attention in recent years [2–5]. A surface magnetoplasmon (SMP) sustained at the interface of a magnetic-optical (MO) and a dielectric material behaves as a one-way EM mode when applying an external dc magnetic field on MO material to break the time-reversal symmetry [6–10]. The one-way SMP was experimentally observed by [11] by using gyromagnetic yttrium-iron-garnet

(YIG) in the microwave regime [11]. Recently, it was reported that one-way SMPs can be used to build a zero-dimensional [12] cavity, which breaks the time-bandwidth limit [13], and the study by Mann *et al* demonstrates that for overcoming the time-bandwidth limit, time-varying systems or nonlinearities are required [14]. More recently, we proposed a high-quality subwavelength isolator based on remanence (we note that remanence has been widely used in industry [15]) and we theoretically investigated this one-way SMP [16]. The one-way feature of the SMP mode provides a promising way to realize light focusing, because it suppresses the reflections.

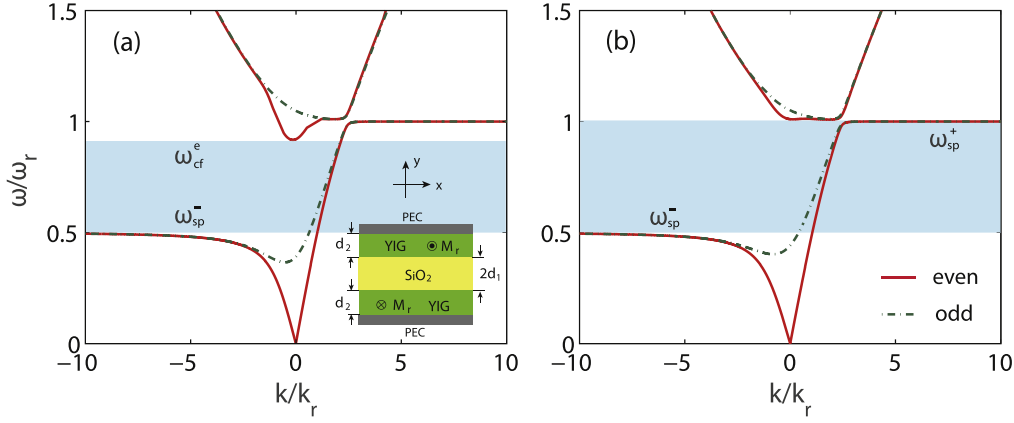


**Figure 1.** The solid and dashed–dotted lines respectively represent the dispersion curves of the ES and OS modes as (a)  $d_1 = d_2 = 0.2\lambda_r$ , (b)  $d_1 = 0.16\lambda_r$  and  $d_2 = 0.2\lambda_r$ . The shaded areas are the COWP regions. Inset: the schematic of the MYDYM structure. The other parameters are  $\epsilon_r = 2.25$ ,  $\epsilon_m = 15$  and  $\omega_r = 2\pi \times 3.587 \times 10^9 \text{ rad s}^{-1}$ .

In traditional optics, light focusing suffers from the diffraction limit. It was reported that surface plasmon polaritons (SPPs) [17–22] or spoof plasmon polaritons [23, 24] or channel plasmon polaritons [25–28] can achieve subwavelength focusing, in which this limit is overcome. One of the main advantages of subwavelength focusing is EM field enhancement. Most previous works focused on the enhanced electric field, instead of the magnetic field [10, 29, 30]. Moreover, the efficiency of the energy localization previously demonstrated is relatively low because of the strong reflection, substantial radiation loss, or both.

In this paper, we theoretically analyze and design a three-dimensional (3D) straight-tapered low-loss one-way waveguide based on remanence to achieve subwavelength focusing. After carefully analyzing the propagation properties of the guided modes in both lossless and lossy conditions, we set up a tapered configuration with an ultra-subwavelength open end surface in the wave propagation direction to achieve ultra-subwavelength focusing. Moreover, we perform wave propagation simulations by using the software COMSOL. As a result, we find that the electric field is enhanced dozens of times, but most importantly, for the first time, we present an extremely enhanced magnetic field with an amplitude enhanced by five orders of magnitude. This approach is useful for obtaining extremely strong magnetic fields both for scientific study and for practical applications, for example, magnetic fluorescence [31].

## 2. One-way waveguide based on remanence

We first study a straight waveguide which is a symmetric waveguide consisting of two YIG layers with opposed magnetization directions and separated by a dielectric layer. In this paper, the dielectric is assumed to be glass with the (relative) permittivity  $\epsilon_r = 2.25$  [32]. As shown in the inset of figure 1(a), the waveguide is covered in the  $y$ -direction by metal layers, which can be treated as perfect electric conductor at microwave frequencies. In this metal-yig-dielectric-yig-metal (MYDYM) model, because of the ferromagnetic

properties, YIG layers still possess gyromagnetic properties after removing the external dc magnetic field and the (relative) permeability of YIG in the  $xyz$  basis takes the form

$$\bar{\mu} = \begin{bmatrix} \mu & -ik & 0 \\ ik & \mu & 0 \\ 0 & 0 & 1 \end{bmatrix}, \quad (1)$$

where  $\mu = 1$ ,  $k = -\omega_r/\omega$  ( $\omega$  is the angular frequency). The parameters  $\mu_0$ ,  $\gamma$ ,  $M_r$  and  $\omega_r = \mu_0\gamma M_r$  are the vacuum permeability, the gyromagnetic ratio, the remanent magnetization and the characteristic circular frequency, respectively. In the proposed structure, the SMPs are transverse-electric-polarized (TE) [33], and based on the distribution of the electric field, they can be divided into two kinds of EM modes, i.e. even-symmetry (ES) and odd-symmetry (OS) modes. Derived from Maxwell's equations and the boundary conditions, the dispersion relations of the ES and OS modes can be respectively written as

$$\mu_2 k_x + \frac{\alpha_2}{\tanh(\alpha_2 d_2)} + \alpha_1 \mu_v \tanh(\alpha_1 d_1) = 0, \quad (\text{even mode}), \quad (2a)$$

$$\mu_2 k_x + \frac{\alpha_2}{\tanh(\alpha_2 d_2)} + \frac{\alpha_1 \mu_v}{\tanh(\alpha_1 d_1)} = 0, \quad (\text{odd mode}), \quad (2b)$$

where  $d_2$  and  $d_1$  represent the thicknesses of the YIG and dielectric layers. The variable  $k_x$  is the propagation constant,  $\alpha_1 = \sqrt{k_x^2 - \epsilon_r k_0^2}$  (where  $k_0 = \omega/c$ ,  $c$  is the speed of light in vacuum) and  $\alpha_2 = \sqrt{k_x^2 - \epsilon_m \mu_v k_0^2}$  (where  $\epsilon_m$  and  $\mu_v = \mu - k^2/\mu$  are the permittivity and the Voigt permeability of YIG, respectively). From equations (2a) and (2b), one can easily calculate the asymptotic frequencies of the ES and OS modes for the two opposite propagation directions, i.e.

$$\omega_{\text{sp}}^- = 0.5\omega_r, \quad (3a)$$

for  $k_x \rightarrow -\infty$  and

$$\omega_{\text{sp}}^+ = \omega_r, \quad (3b)$$

for  $k_x \rightarrow +\infty$ . It should be noted that  $\omega_{\text{sp}}^-$  and  $\omega_{\text{sp}}^+$  are the same for both the ES and OS modes. For convenience, we introduce

a waveguide parameter  $D = (d_1, d_2)$  (which is actually a vector of two parameters). In figure 1(a), the solid and dashed-dotted lines respectively represent the dispersion curves of the ES and OS modes as  $D = (0.2\lambda_r, 0.2\lambda_r)$  (where  $\lambda_r$  equals  $2\pi c / \omega_r$ ). Throughout this paper, the characteristic remanent circular frequency and the permittivity of YIG are assumed to be  $\omega_r = 2\pi \times 3.587 \times 10^9 \text{ rad s}^{-1}$  and  $\epsilon_m = 15$  [15], respectively. The shaded area in figure 1(a) represents the complete one-way propagation (COWP) region and it obviously suffers from the high-frequency branch (the higher branch shown in figure 1(a)) of the ES modes. Although it is difficult to directly obtain the cutoff frequency ( $\omega_{cf}^e$ ) of the high-frequency branch of the ES modes by solving equation (2a), the frequency  $\omega_{cf}^e$  does not deviate much from the solution of equation (2a) in the limit  $k_x \rightarrow 0$ . When considering the asymptotic frequency (AF) band ( $\omega_{sp}^-, \omega_{sp}^+$ ), we have  $\alpha_2 > 0$  for  $\mu_v < 0$ , and  $\alpha_1 = ik_1$  with  $k_1 = \sqrt{\epsilon_r} k_0$  as  $k_x = 0$  and equation (2a) changes into

$$\frac{\alpha_2}{\tanh(\alpha_2 d_2)} - k_1 \mu_v \tan(k_1 d_1) = 0. \quad (4)$$

In equation (4), the value of the first term is always greater than zero. Therefore, equation (4) has no solution as  $k_1 d_1 < \pi/2$  in the AF band. Here, we introduce a critical thickness  $d_c$  as  $k_1 d_1 = \pi/2$  and  $\omega_{cf}^e$  should be larger than  $\omega_{sp}^+$  when  $d_1 < d_c$ . The critical thickness  $d_c$  can be rewritten in the form

$$d_c = \frac{1}{4\sqrt{\epsilon_r}} \lambda_r. \quad (5)$$

In this paper,  $d_c \approx 0.166\lambda_r$  (for  $\lambda_r \approx 83.6 \text{ mm}$ ) and figure 1(b) shows the dispersion curves of the ES and OS modes as  $D = (0.16\lambda_r, 0.2\lambda_r)$  in which  $d_1$  is smaller than  $d_c$ . As a result, in figure 1(b) the COWP band is the whole AF band and we emphasize that the width of the COWP band in this case is maximal.

Furthermore, one can see from figure 1 that the low-frequency branch of the dispersion curves of the OS modes has a relative small cutoff frequency  $\omega_{cf}^o$  ( $\omega_{cf}^o < \omega_{sp}^-$ ). We further investigate the relation between the dispersion curves of the OS modes and the waveguide parameter  $D$  in figure 2(a), in which two horizontal dashed lines represent the asymptotic frequencies of the OS modes. Figures 2(b) and (c) show the group velocity ( $v_g$ ) of the OS modes as functions of  $k_x$  and  $\omega$ . It is clear that for smaller  $d_1$ , e.g. for  $d_1 = 0.01\lambda_r$ ,  $v_g$  is continuously larger than zero and  $\omega_{cf}^o = \omega_{sp}^-$ . By contrast, in the cases  $D_1$  and  $D_2$ ,  $\omega_{cf}^o < \omega_{sp}^-$  and  $v_g$  becomes negative in some frequencies below the AF band. Moreover,  $v_g$  (in the AF band) in the  $D_1/D_2$  cases is larger than for the  $D_3/D_4$  cases, as shown in figure 2(c). On the other hand, comparing the cases with the same  $d_1$  value, i.e.  $D_1/D_3$  and  $D_2/D_4$ ,  $v_g$  increases in the AF band when  $d_2$  changes from  $0.01\lambda_r$  to  $0.1\lambda_r$ . The ability of changing group velocity by simply changing the thickness of the YIG or the dielectric can be used to slow down or accelerate the propagation of EM modes. However, in this paper we just concentrate on the subwavelength focusing.

Since it seems that  $\omega_{cf}^o = \omega_{sp}^-$  holds for cases with small values of  $d_1$  in figure 2, we plot figure 3 that shows the

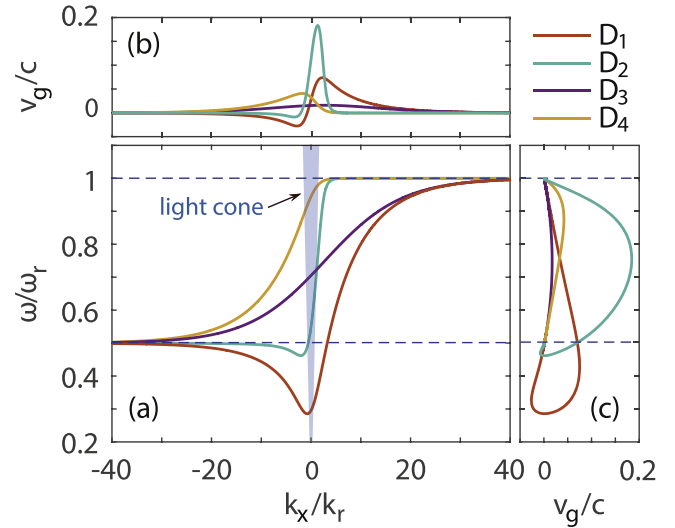


**Figure 2.** (a) The dispersion curves and (b), (c) the group velocities of the OS modes. The solid lines from bottom to top represent  $D_1 = (0.1\lambda_r, 0.01\lambda_r)$ ,  $D_2 = (0.1\lambda_r, 0.1\lambda_r)$ ,  $D_3 = (0.01\lambda_r, 0.01\lambda_r)$  and  $D_4 = (0.01\lambda_r, 0.1\lambda_r)$ , respectively. The two horizontal lines represent the two asymptotic frequencies  $\omega_{sp}^\pm$  of equation (3a) of the OS modes. The shaded zone is the light cone of the glass. The other parameters are the same as in figure 1.

functional relation between  $\omega_{cf}^o$  and  $d_1$  for different values of  $d_2$ . In accordance with the above discussion of figure 2, in figure 3(a) when  $d_2$  increases,  $\omega_{cf}^o$  increases and when  $d_1$  increases, then  $\omega_{cf}^o$  decreases, except for small  $d_1$  cases in which  $\omega_{cf}^o = \omega_{sp}^-$ . We further demonstrate the numerical values of  $d_1$  and  $d_2$  as  $\omega_{cf}^o = \omega_{sp}^-$  as the red line shown in figure 3(b). For clarity, in figure 3(b) we shade the left and right areas of the red line, and the green and gray areas respectively represent the OS modes with  $\omega_{cf}^o = \omega_{sp}^-$  and  $\omega_{cf}^o \leq \omega_{sp}^-$ . We emphasize that for large  $d_1$  cases, for example  $d_1 = 0.1\lambda_r$ ,  $\omega_{cf}^o \leq \omega_{sp}^-$  permanently holds for all values of  $d_2$ . However, in this paper, we only consider the small  $d_1$  cases ( $d_1 < 0.01\lambda_r$ ) for designing ultra-subwavelength focusing waveguides.

### 3. Ultra-subwavelength focusing waveguide

In the above analysis, we ignored the loss in the waveguide which should be a good approximation in calculating the dispersion relation [16, 34, 35]. However, when designing a waveguide, loss should be carefully studied. In the lossy YIG material (see chapter 9 in [15]),  $k$  and  $\mu$  in equation (1) become

$$\mu = 1 + \frac{i\nu\omega_r}{\omega^2 + \nu^2}, \quad (6)$$

$$k = -\frac{\omega\omega_r}{\omega^2 + \nu^2}, \quad (7)$$

where  $\nu$  is the relaxation angular frequency (in this paper, we set  $\nu = 10^{-3}\omega$ ). In this lossy model, the propagation constant in equations (2) and (3) now becomes a complex number,

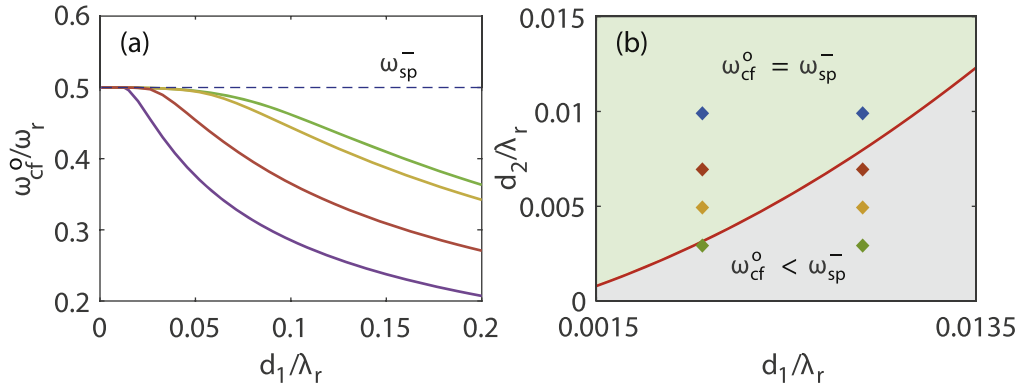


**Figure 3.** (a) The functional dependence of  $\omega_{cf}^o$  on  $d_1$  as  $d_2$  is kept constant. Purple line:  $d_2 = 0.01\lambda_r$ ; red line:  $d_2 = 0.02\lambda_r$ ; yellow line:  $d_2 = 0.05\lambda_r$ ; green line:  $d_2 = 0.1\lambda_r$ . (b) The  $(d_1, d_2)$  space divided into two areas, i.e. the green shaded area and the gray shaded area and they represent  $\omega_{cf}^o = \omega_{sp}^-$  and  $\omega_{cf}^o < \omega_{sp}^-$ , respectively.

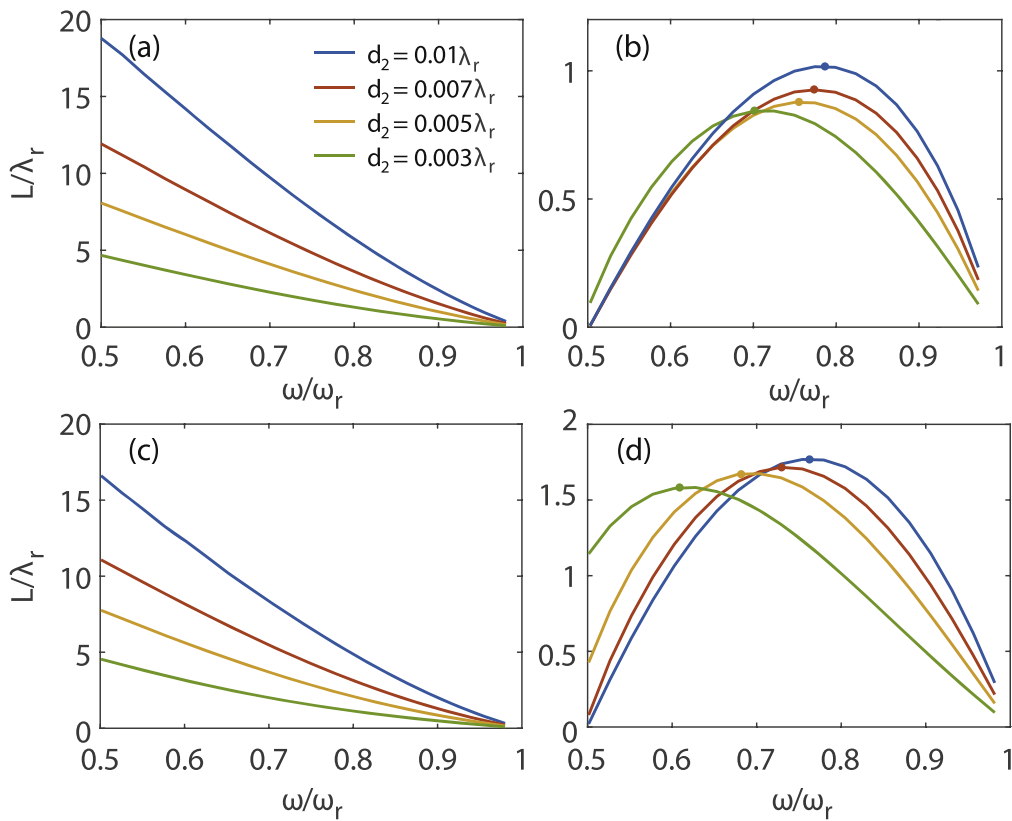


**Figure 4.** (a), (c) The  $L$  of the ES modes in the band  $(\omega_{sp}^-, \omega_{sp}^+)$  with  $d_1 = 0.005\lambda_r$  in (a) and  $d_1 = 0.01\lambda_r$  in (c). (b), (d) The  $L$  of the OS modes with  $d_1 = 0.005\lambda_r$  in (b) and  $d_1 = 0.01\lambda_r$  in (d). The relaxation angular frequency  $\nu = 10^{-3}\omega$ .

i.e.  $k_x = k_r + ik_i$ . The propagation length ( $L$ ) is defined by  $L = 1/(2k_i)$ . Figure 4 shows the  $L$  as a function of the angular frequency  $\omega$  for different waveguide parameters  $D$ . Four colored lines in figure 4 represent four different values of  $d_2$  as the insert legend shows in figure 4(a). Figures 4(a), (c) and (b), (d) represent the  $L$  of the ES and OS modes, respectively. Moreover, figures 4(a), (b) and (c), (d) have different values of  $d_1$ , i.e.  $d_1 = 0.005\lambda_r$  in (a) and (b), and  $d_1 = 0.01\lambda_r$  in (c) and (d). As seen in figures 4(a) and (c), for the ES modes, the lower the frequency or the thicker the YIG layer, the longer the propagation length. Figures 4(b) and (d) show that for the

OS modes, the longest  $L$  (the marked points) happens at  $0.5\omega_r < \omega < \omega_r$  and a ‘redshift’ occurs as  $d_2$  decreases. In figures 4(b) and (d), when  $\omega \rightarrow 0.5\omega_r$  ( $\omega_{sp}^-$ ) the  $L$  in some cases vanishes, which can be understood when we look back to figure 3(b). In figure 3(b), the left/right four diamonds represent the four parameters in figures 4(b) and (d) and for those diamonds located in the green area with  $\omega_{cf}^o = \omega_{sp}^-$ , we have  $k_r \rightarrow \infty$ , further,  $k_i \rightarrow \infty$  and  $L \rightarrow 0$ , which indeed agree with the results shown in figures 4(b) and (d). Most importantly, comparing the four panels in figure 4, one can see that the  $L$  of the ES modes can be several or even dozens

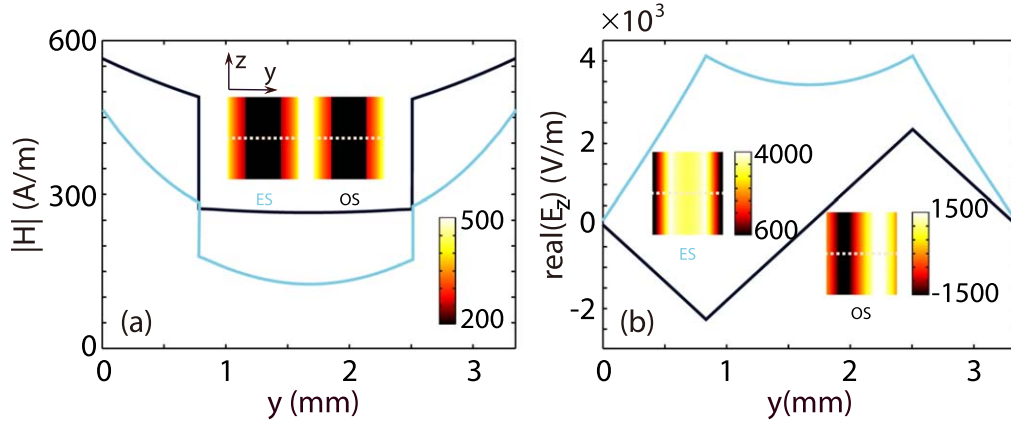


**Figure 5.** (a) The magnetic-field amplitude and (b) the real part of the electric-field amplitude of the ES modes (cyan lines) and the OS mode (black lines) along the dotted lines shown in the insets. The other parameters are  $D = (0.01\lambda_r, 0.01\lambda_r)$  and  $\omega = 0.75\omega_r$ .

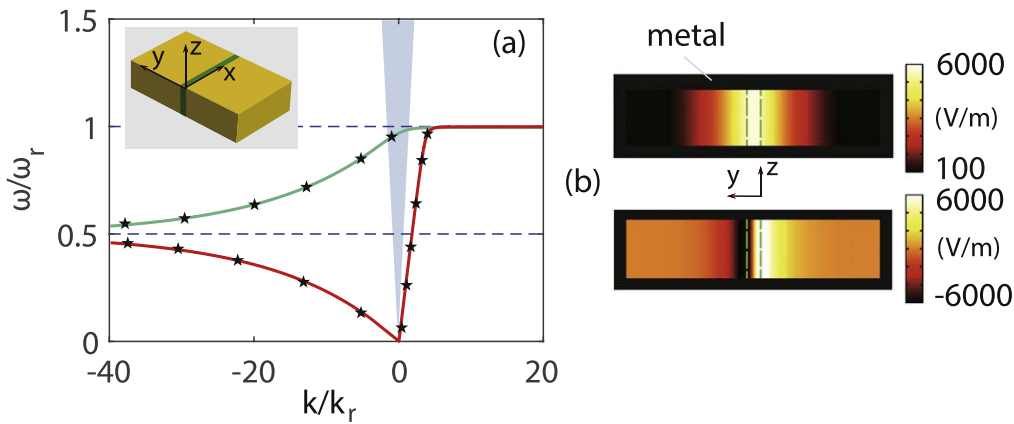


**Figure 6.** (a) The solid lines represent the dispersion curves of a 2D MYDYM waveguide as  $d_1 = 0.005\lambda_r$  and  $d_2 = 0.1\lambda_r$ , and the stars are the eigenmode solutions of the corresponding 3D model. The inset is the schematic structure of the 3D model and the height is set to be  $h_1 = 4$  mm. (b) The electric-field ( $E_z$ ) distribution of the ES (top) and OS (bottom) eigenmodes in the 3D model. The other parameters are the same as in figure 1.

of times larger than the one of the OS modes. In other words, the ES modes propagate in the waveguide with much lower loss than the OS modes.

To further explain the low-loss propagation property of the ES modes, we solve the eigen-field distributions when the energy flux density is the same in the cross section (the YZ plane) for both the ES and OS modes in figure 5. The parameters are  $D = (0.01\lambda_r, 0.01\lambda_r)$  and  $\omega = 0.75\omega_r$  which is the center frequency of the AF band. The cyan and black lines in figure 5(a) respectively represent the magnetic-field amplitude  $|H|$  of the ES and OS modes along the dotted lines shown in the inset. Figure 5(b) is the corresponding real part of the electric field  $E_z$  of the ES and OS modes. It is obvious in figure 5(a) that  $|H|$  of the ES modes is smaller than the one of the OS modes in the YIG layers. In our calculation, about 54% of the EM energy is confined in the YIG layers for the ES modes. By contrast, this value is nearly 94% for the OS modes. Due to the gyromagnetic properties of YIG, the higher energy ratio in YIG will lead to a shorter propagation length. Therefore, we choose the ES modes as our preferred guided modes in designing the 3D subwavelength waveguide.

In figure 6(a), we compare the dispersion relation in straight uniform 2D and 3D models (see the inset) when the

waveguide parameter  $D$  is the same in the two models. The red (cyan) line and stars respectively represent the dispersion curves of the ES (OS) modes solved in lossless 2D and 3D models. Note that in this paper, the 3D waveguides in the  $y$ - and  $z$ -directions are terminated by metal layers and for convenience, we only show the YIG-glass-YIG structure in all schematic structures of 3D models. We choose the waveguide parameter  $D = (0.005\lambda_r, 0.1\lambda_r)$  because in the lossy 2D model with  $\nu = 10^{-3}\omega$ , the propagation loss is extremely low and the propagation length exceeds  $100\lambda_r$  as  $\omega = 0.75\omega_r$ . The propagation properties of 2D and 3D configurations are quite similar. This is because the EM modes in the proposed models are TE modes and the non-zero electric field is  $E_z$ , which is perpendicular to the metal layers in the  $z$ -direction. Therefore, the EM mode distribution is almost the same for both 2D and 3D models. In figure 6(b), we show the electric ( $E_z$ ) distribution of ES (top) and OS (bottom) eigenmodes in the cross section of the 3D model, and one can see that  $E_z$  is uniform in the  $z$ -direction.

Inspired by the analyses of figures 4–6, we propose that in the COWP band ( $\omega_{sp}^-, \omega_{sp}^+$ ), low-loss one-way 3D waveguides can be realized, and we further use this waveguide to achieve subwavelength focusing. In previous subwavelength

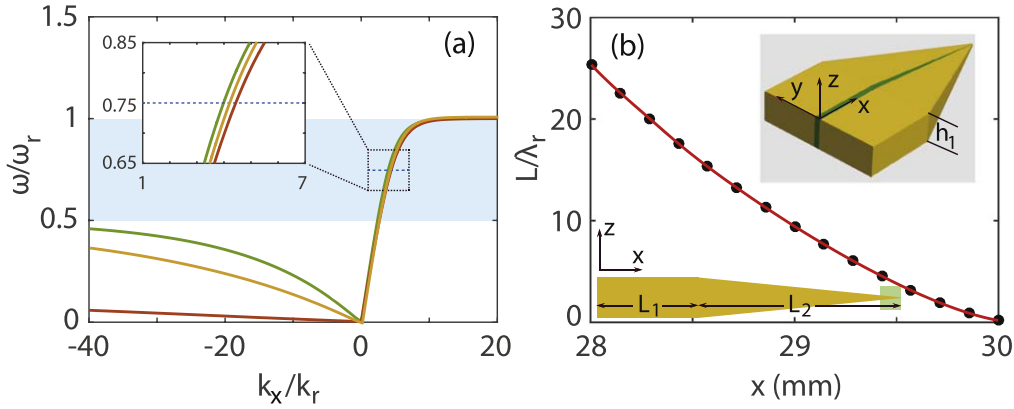


**Figure 7.** (a) The dispersion curves of the ES modes as  $x = 10$  mm (the green lines),  $x = 20$  mm (the yellow lines) and  $x = 30$  mm (the red lines). (b) The  $L$  of the 3D model as  $\omega = 0.75\omega_r$  as  $28 < x < 30$  mm, i.e. the shaded green area shown in the left inset. The two insets show the schematic of the designed tapered 3D structure which consists of a straight part with length  $L_1 = 10$  mm and a tapered part with length  $L_2 = 20$  mm. The relaxation angular frequency is set to be  $\nu = 10^{-3}\omega$ .

focusing works [10, 22], the focusing scale is always  $\sim 10^{-2}\lambda_0$  ( $\lambda_0$  is the wavelength in vacuum), and ultra-subwavelength ( $\sim 10^{-4}\lambda_0$ ) focusing has never been achieved. Here, we propose a joint straight-tapered waveguide as the insets shown in figure 7(b). The parameters of the straight part are  $D = (0.005\lambda_r, 0.1\lambda_r)$ ,  $L_1 = 10$  mm (the length of the straight part) and  $h_1 = 4$  mm (the height of the straight part). The end surface of the tapered part has the parameters  $d_1 = d_2 = 2 \times 10^{-4}\lambda_r$  ( $\sim 10^{-4}\lambda_0$ ,  $\lambda_0 \approx 111.5$  mm as  $\omega = 0.75\omega_r$ ) and  $h_2 \approx 1.8 \times 10^{-4}\lambda_r$  ( $\sim 10^{-4}\lambda_0$ ). The length of the tapered part is  $L_2 = 20$  mm. Figure 7(a) shows the dispersion curves of the ES modes in the tapered part as  $x = 10$  mm (the green lines),  $x = 20$  mm (the yellow lines) and  $x = 30$  mm (the red lines). One can easily see from figure 7(a) that the ES modes propagating in the tapered part still possess the one-way propagation properties in the whole AF band. To further demonstrate the propagation loss in the waveguide, we numerically calculate the  $L$  in the region  $28 \text{ mm} \leq x \leq 30$  mm corresponding to the green shaded area in the left inset in figure 7(b) for  $\omega = 0.75\omega_r$  (see the horizontal lines in figure 7(a)). As a result, we find a propagation length  $L \approx 800$  mm as  $x = 29$  mm. That is only 1 mm away from the end surface and even at the end surface ( $x = 30$  mm)  $L$  still has a value of around 11 mm. In this designed structure, because of one-way low-loss propagation, one can expect significantly enhanced fields in the near-field region of the end surface.

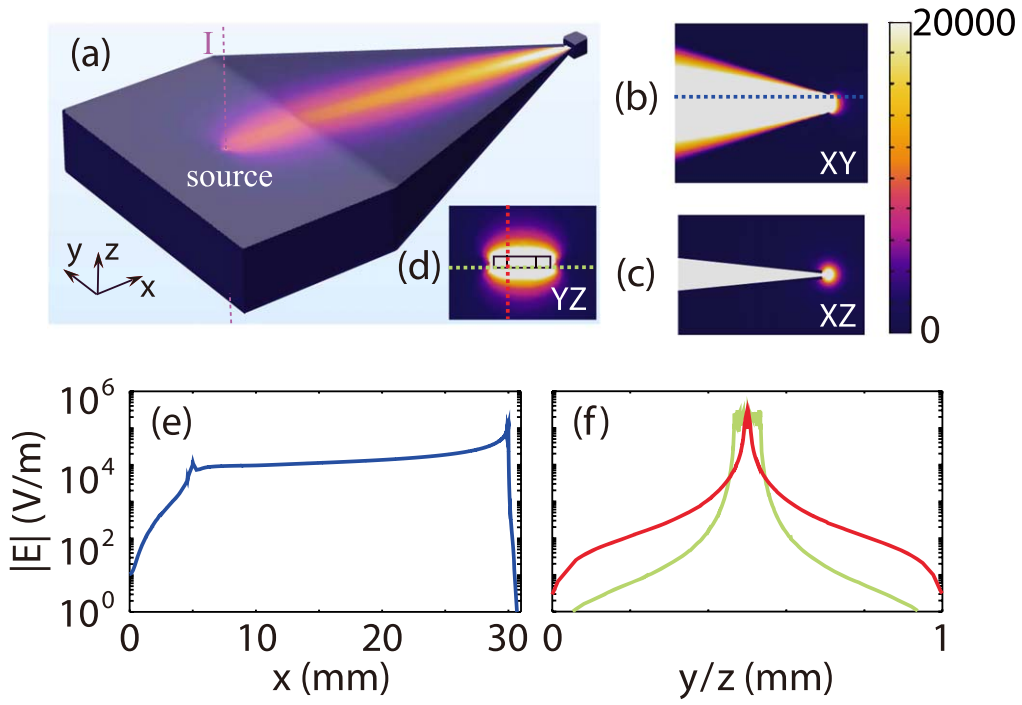
#### 4. Extremely enhanced magnetic field

By using the commercial finite-element software COMSOL Multiphysics, we simulate the wave propagation in the above joint waveguide system at  $\omega = 0.75\omega_r$  with  $\nu = 10^{-3}\omega$ . As seen in figure 8(a), we set a line current source ( $I = 1$  A) in the middle of the glass layer to excite the ES modes and the coordinates of the source are  $x = 5$  mm and  $y = d_1$ . Figure 8(a) demonstrates the electric-field amplitude ( $|E|$ ) distribution. As we expect, the excited mode propagates along the  $+x$  direction with no interference even in the tapered

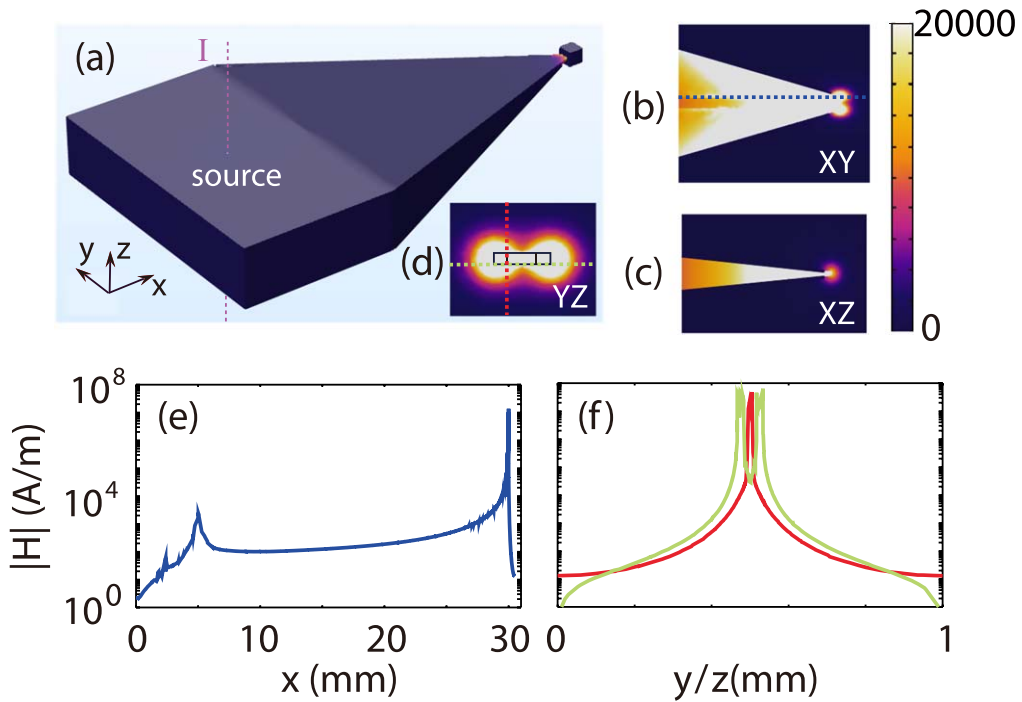
waveguide part. Figures 8(b)–(d) show the zoom-in electric-field distributions in the  $XY$  ( $z = -h_1/2$ ),  $XZ$  ( $y = d_1$ ) and  $YZ$  (the end surface,  $x = 30$  mm) planes. It is quite clear that the electric field is focused in the near-field region around the end surface. Figure 8(e) shows  $|E|$  along the dashed line in figure 8(b) and we find that the electric field is enhanced dozens of times near  $x = 30$  mm compared with the value in the straight (i.e. non-tapered) waveguide. Similarly, in figure 8(f) the green and red lines respectively show the electric-field distribution along the green and red dashed lines marked in figure 8(d). Through figure 8(f), we can immediately calculate the full widths at half maximum (FWHM) of the focused electric field on the end surface to be  $\text{FWHM}_y \approx 0.1$  mm ( $\approx 9 \times 10^{-4}\lambda_0$ ) and  $\text{FWHM}_z \approx 0.04$  mm ( $\approx 3.6 \times 10^{-4}\lambda_0$ ).

Figure 9, being similar to figure 8, shows the corresponding simulation results for the magnetic field. In figure 9(a), the magnetic field is focused at the end of the waveguide. Figures 9(b)–(d) are the magnetic-field distributions in the same planes corresponding to figures 8(b)–(d). Because YIG is a ferromagnetic material, the magnetic field near the YIG layers will be larger than the one near glass or air as seen in figure 9(b) (the heart-shaped magnetic field distribution), figure 9(d) (the dumbbell-shaped magnetic field distribution) and figure 9(f) (the green line with double peaks). Figure 9(f) shows the distribution of the focused magnetic field on the end surface along the dashed lines shown in figure 9(d). As one of our main results shown in figure 9(e), which is the magnetic-field amplitude along the dashed line shown in figure 9(b), the magnetic-field amplitude is extremely enhanced by a few hundred thousand times near  $x = 30$  mm compared to the straight waveguide. As far as we know, this giant enhancement has never been achieved before.

In addition, we further demonstrate the transmission efficiency and the loss by lengthening the previous model properly. In the lengthened model, the end surface for power output protrudes from the previous structure by using a thin straight (one-way) waveguide of the length  $L_3 = 1$  mm (see the inset in figure 10(b)). Figure 10(a) shows the simulated electric-field amplitudes in the  $XY$  plane ( $z = -h_1/2$ ).



**Figure 8.** (a) The electric-field amplitude  $|E|$  distribution in the designed 3D waveguide. The zoom magnified pictures of (a) near the end surface of the waveguide in (b) the  $XY$  plane ( $z = -h_1/2$ ) and (c) the  $XZ$  plane ( $y = d_1$ ). (d) The electric-field distribution on the end surface ( $x = 30$  mm). (e) The electric-field amplitude along the dashed line shown in (b). (f) The electric-field amplitude along the dashed lines shown in (d).



**Figure 9.** (a)–(d) Same as in figure 8 except for the field shown in this figure is the magnetic field. (e), (f) The magnetic field around the end surface is enhanced by five orders of magnitude compared to the straight waveguide.

According to the results of figures 4 and 7, the EM mode in this configuration will propagate to the end with more loss, and this can be seen in figure 10(b): the absolute value of the slope of the normalized power flows gradually increases

along the  $+x$  direction. However, the power efficiency remained about 93% at  $x = 30$  mm, which implies the joint waveguide system in figures 7–9 is truly low-loss for the ES modes in the COWP band. Moreover, the propagation loss



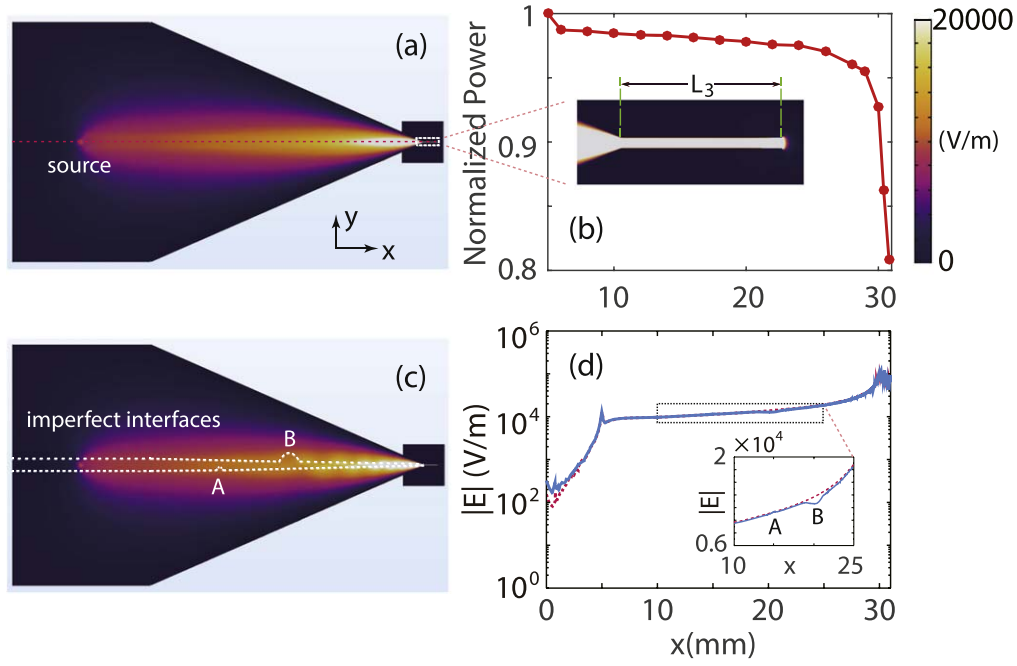


**Figure 10.** (a) Electric-field amplitudes in the lengthened (3D) structure with thin protruded waveguide of the length  $L_3 = 1$  mm. (b) Normalized power along the  $+x$  direction. The inset in (b) is the zoom-in picture on the protruded part. (c) Electric-field amplitudes in the structure with imperfections (marked by A and B). The white dashed lines indicate the glass-YIG interfaces. (d) Distribution of the electric-field amplitude along the central axis of the structure, which is indicated by a dashed line in (a). The solid and dotted lines correspond to the results for the cases with and without imperfection, respectively. The inset shows the zoom-in picture on the region around the imperfections.

between  $x = 30$  mm and  $x = 31$  mm is around 10%, which fits well with the results in figure 7(b). Immunity to back-scattering is one of the most important features for one-way waveguide. Based on this feature, the proposed focusing system should be fairly insensitive to fabrication imperfection. To show this, we introduce two imperfections into the system shown in figure 10(a) and perform the simulation of wave transmission in it. The two imperfections respectively lie at the lower and upper glass-YIG interfaces, and they are separated by a distance of 5 mm. The lower imperfection (marked by A) at  $x = 15$  mm is a semi-circular column of YIG with the radius  $r_1 = 0.3$  mm, and the upper one (marked by B) at  $x = 20$  mm is a semi-circular column of glass with the radius  $r_2 = 0.8$  mm (see figure 10(c)). The simulated electric-field amplitudes are plotted in figure 10(c), which is similar to figure 10(a) for the case without imperfection. Figure 10(d) shows the field distribution along the central axis of the system, which is marked by a (red) dashed line in figure 10(a), and the corresponding results for the case without imperfection are also included in it for comparison. The inset in figure 10(d) is the zooming in on the local region including the two imperfections. Obviously, the fields of SMPs are only modified locally in the presence of the imperfections, and they quickly recover behind the imperfections (for  $x > 25$  mm), which are almost the same as that for the case without imperfection. This approach to obtain extremely enhanced magnetic fields can be used in numerous fields including but not limited to magnetic field enhanced or

quenched fluorescence, luminescence in 2D materials and novel optical tips for near-field microwave microscopy.

## 5. Conclusion and outlook

In conclusion, we propose a 3D joint straight-tapered MYDYM waveguide based on remanence to achieve ultra-subwavelength ( $\sim 10^{-4} \lambda_0 \times 10^{-4} \lambda_0$ ) focusing at microwave frequencies. We theoretically analyze the propagation properties of the ES and OS modes in the MYDYM structure, and compared to the OS modes, the ES modes propagate with much lower loss. When the thicknesses of the YIG layer and dielectric layer are identical, we find that the dispersion relation in the 3D model is almost the same as the one in the 2D model. By using the software COMSOL, we perform wave propagation simulations in the designed 3D model as  $\omega = 0.75\omega_r$  (the center frequency of the COWP band). As we expected, the EM fields are confined in the tapered part and the electric field is enhanced dozens of times. More interestingly, in this case, the enhanced magnetic-field amplitude is enhanced up to five orders of magnitude. In addition, we further investigate the propagation loss in an extended tapered waveguide. The ES mode propagating in this waveguide is proved to be low-loss and the efficiency of the power in the simulation is about 93% at the  $x = 30$  mm (the end surface of the previous waveguide). It should be noted that the mechanism mentioned in this paper can be expanded to the

terahertz regime [9] once the equivalent perfect-magnetic-conductor is built, for example by using metamaterials [36].


## Funding information

We acknowledge support by National Natural Science Foundation of China (NSFC) (61372005), National Natural Science Foundation of China (NSFC) under a key project (41331070), and Independent Research Fund Denmark (9041-00333B). The Center for Nanostructured Graphene is sponsored by the Danish National Research Foundation (Project No. DNR103).

## ORCID iDs

Martijn Wubs  <https://orcid.org/0000-0002-8286-7825>

Sanshui Xiao  <https://orcid.org/0000-0001-6529-5047>

Linfang Shen  <https://orcid.org/0000-0002-3602-515X>

## References

- [1] Prange R E and Girvin S M 1987 *The Quantum Hall Effect* (Berlin: Springer)
- [2] Haldane F D M and Raghu S 2008 Possible realization of directional optical waveguides in photonic crystals with broken time-reversal symmetry *Phys. Rev. Lett.* **100** 013904
- [3] Skirlo S A, Lu L and Soljačić M 2014 Multimode one-way waveguides of large Chern numbers *Phys. Rev. Lett.* **113** 113904
- [4] Lu L, Joannopoulos J D and Soljačić M 2014 Topological photonics *Nat. Photon.* **8** 821
- [5] Khanikaev A B and Shvets G 2017 Two-dimensional topological photonics *Nat. Photon.* **11** 763
- [6] Raghu S and Haldane F D M 2008 Analogs of quantum-Hall-effect edge states in photonic crystals *Phys. Rev. A* **78** 033834
- [7] Wang Z, Chong Y D, Joannopoulos J D and Soljačić M 2008 Reflection-free one-way edge modes in a gyromagnetic photonic crystal *Phys. Rev. Lett.* **100** 013905
- [8] Ao X, Lin Z and Chan C T 2009 One-way edge mode in a magneto-optical honeycomb photonic crystal *Phys. Rev. B* **80** 033105
- [9] Xu J, Xiao S, Wu C, Zhang H, Deng X and Shen L 2019 Broadband one-way propagation and rainbow trapping of terahertz radiations *Opt. Express* **27** 10659–69
- [10] Shen Q, Hong L, Deng X and Shen L 2018 Completely stopping microwaves with extremely enhanced magnetic fields *Sci. Rep.* **8** 15811
- [11] Wang Z, Chong Y, Joannopoulos J D and Soljačić M 2009 Observation of unidirectional backscattering-immune topological electromagnetic states *Nature* **461** 772
- [12] Dutra S M 2005 *Cavity Quantum Electrodynamics: The Strange Theory of Light in a Box* (New York: Wiley)
- [13] Tsakmakidis K, Shen L, Schulz S, Zheng X, Upham J, Deng X, Altug H, Vakakis A F and Boyd R 2017 Breaking Lorentz reciprocity to overcome the time-bandwidth limit in physics and engineering *Science* **356** 1260–4
- [14] Mann S A, Sounas D L and Alù A 2019 Nonreciprocal cavities and the time-bandwidth limit *Optica* **6** 104–10
- [15] Pozar D M 2011 *Microwave Engineering* (New York: Wiley)
- [16] You Y, Xiao S, Wu C, Zhang H, Deng X and Shen L 2019 Unidirectional-propagating surface magnetoplasmon based on remanence and its application for subwavelength isolators *Opt. Mater. Express* **9** 2415–25
- [17] Stockman M I 2004 Nanofocusing of optical energy in tapered plasmonic waveguides *Phys. Rev. Lett.* **93** 137404
- [18] Yin L, Vlasko-Vlasov V K, Pearson J, Hiller J M, Hua J, Welp U, Brown D E and Kimball C W 2005 Subwavelength focusing and guiding of surface plasmons *Nano Lett.* **5** 1399–402
- [19] Steele J M, Liu Z, Wang Y and Zhang X 2006 Resonant and non-resonant generation and focusing of surface plasmons with circular gratings *Opt. Express* **14** 5664–70
- [20] Desiatov B, Goykhman I and Levy U 2011 Plasmonic nanofocusing of light in an integrated silicon photonics platform *Opt. Express* **19** 13150–7
- [21] Choo H, Kim M-K, Staffaroni M, Seok T J, Bokor J, Cabrini S, Schuck P J, Wu M C and Yablonovitch E 2012 Nanofocusing in a metal-insulator-metal gap plasmon waveguide with a three-dimensional linear taper *Nat. Photon.* **6** 838
- [22] He X, Yang L and Yang T 2011 Optical nanofocusing by tapering coupled photonic-plasmonic waveguides *Opt. Express* **19** 12865–72
- [23] Maier S A, Andrews S R, Martín-Moreno L and García-Vidal F J 2006 Terahertz surface plasmon-polariton propagation and focusing on periodically corrugated metal wires *Phys. Rev. Lett.* **97** 176805
- [24] Zhang H C, Cui T J, Zhang Q, Fan Y and Fu X 2015 Breaking the challenge of signal integrity using time-domain spoof surface plasmon polaritons *ACS Photonics* **2** 1333–40
- [25] Volkov V S, Bozhevolnyi S I, Rodrigo S G, Martín-Moreno L, García-Vidal F J, Devaux E and Ebbesen T W 2009 Nanofocusing with channel plasmon polaritons *Nano Lett.* **9** 1278–82
- [26] Smith C L, Thilsted A H, Garcia-Ortiz C E, Radko I P, Marie R, Jeppesen C, Vannahme C, Bozhevolnyi S I and Kristensen A 2014 Efficient excitation of channel plasmons in tailored, UV-lithography-defined v-grooves *Nano Lett.* **14** 1659–64
- [27] Moreno E, Garcia-Vidal F, Rodrigo S G, Martín-Moreno L and Bozhevolnyi S I 2006 Channel plasmon-polaritons: modal shape, dispersion, and losses *Opt. Lett.* **31** 3447–9
- [28] Søndergaard T, Bozhevolnyi S I, Beermann J, Novikov S M, Devaux E and Ebbesen T W 2009 Resonant plasmon nanofocusing by closed tapered gaps *Nano Lett.* **10** 291–5
- [29] Nazir A, Panaro S, Proietti Zaccaria R, Liberale C, De Angelis F and Toma A 2014 Fano coil-type resonance for magnetic hot-spot generation *Nano Lett.* **14** 3166–71
- [30] Mirzaei A and Miroshnichenko A E 2015 Electric and magnetic hotspots in dielectric nanowire dimers *Nanoscale* **7** 5963–8
- [31] Baranov D G, Savelev R S, Li S V, Krasnok A E and Alù A 2017 Modifying magnetic dipole spontaneous emission with nanophotonic structures *Laser Photon. Rev.* **11** 1600268
- [32] Mason D R, Gramotnev D K and Kim K S 2012 Plasmon nanofocusing in a dielectric hemisphere covered in tapered metal film *Opt. Express* **20** 12866–76
- [33] Hartstein A, Burstein E, Maradudin A, Brewer R and Wallis R 1973 Surface polaritons on semi-infinite gyromagnetic media *J. Phys. C: Solid State Phys.* **6** 1266
- [34] Shen L, Zheng X and Deng X 2015 Stopping terahertz radiation without backscattering over a broad band *Opt. Express* **23** 11790–8
- [35] Shen L, Xu J, You Y, Yuan K and Deng X 2017 One-way electromagnetic mode guided by the mechanism of total internal reflection *IEEE Photonics Technol. Lett.* **30** 133–6
- [36] Shahvarpour A and Caloz C 2009 Grounded ferrite perfect magnetic conductor and application to waveguide miniaturization *IEEE-MTTs Int. Microwave Symp. Digest* pp 25–8